The slowly varying corona: I — DEM calculation from EVE MEGS-A spectra and implications for the Fe XVIII 94 Å line

S. J. Schonfeld[1], S. M. White[2], R. A. Hock[2],
and
R. T. J. McAteer[1]

[1]*New Mexico State University, Department of Astronomy, P.O. Box 30001, MSC 4500, Las Cruces, NM 88003-8001, schonfsj@gmail.com*

[2]*Air Force Research Laboratory, Space Vehicles Directorate, AFRL, 3550 Aberdeen Ave SE, Kirtland AFB, Albuquerque, NM 87117*

ABSTRACT

Subject headings: Sun: abundances, Sun: corona, Sun: solar-terrestrial relations, Sun: UV radiation

1. Introduction

In principle it is simple to determine the temperature distribution of coronal plasma by inverting a set of EUV observations sensitive to different plasma temperatures. In practice however, observational noise, finite observations, and incomplete knowledge of the relevant atomic physics make this an ill-posed problem complicated by the details of the algorithmic method used to determine the result. These difficulties have been well understood for decades (Craig & Brown 1976) and considerable effort is still made to validate these differential emission measure (DEM) analyses (Guennou et al. 2012a,b; Testa et al. 2012a; Aschwanden et al. 2015). However, recent years have seen the advent of impressive new DEM calculation techniques (Hannah & Kontar 2012; Plowman et al. 2013; Cheung et al. 2015) which have been validated for a wide range of coronal conditions and run quickly, allowing DEM studies of larger spatial and temporal domains than ever before.

One of the original promises of the Solar Dynamics observatory (Pesnell et al. 2011) was improved understanding of the solar corona through determination of the DEM with both the Atmospheric Imaging Assembly (AIA; Lemen et al. 2012) and the EUV (extreme ultraviolet) Variability Experiment (EVE; Woods et al. 2012). This has been accomplished for studies of solar flares (e.g. Hock 2012; Fletcher et al. 2013; Kennedy et al. 2013; Warren et al. 2013; Caspi et al. 2014; Warren 2014; Zhu et al. 2016), active regions (e.g. Warren et al. 2012; Aschwanden et al. 2013; Del Zanna 2013; Petralia et al. 2014), loops (e.g. Aschwanden & Boerner 2011; Warren et al. 2011; Del Zanna et al. 2011), the full disk (e.g. Nuevo et al. 2015; Schonfeld et al. 2015), and even the full disk over an entire Carrington rotation (Vázquez 2016). The most lauded feature of all SDO observations is their high time resolution, allowing study of transient events such as solar flares (e.g. Hudson et al. 2011; Milligan et al. 2012) with more detail than ever before. But equally important are their consistent, long-term, full-disk observations.

To our knowledge, there has been no study of the long term coronal DEM variability leveraging these uniform data sets to investigate the evolution of the global corona over the solar cycle. Considering the corona in such a holistic sense provides perspectives lost in narrowly focused active region studies. EVE MEGS-A spectra are particularly well suited to this task because extra effort has been made to provide on-flight calibration thanks to sounding rocket under-flights with an identical instrument (CITATION). Additionally, the ability to identify individual emission lines allows for the selection of well characterized regions of the EUV spectrum which is crucial for this kind of analysis where DEM calculations are performed for a wide range of coronal conditions.

We present an analysis of the long term variation of the corona through calculation of daily full disk integrated DEMs utilizing the complete EVE MEGS-A data set. We discuss the instrument and data set in §2 with special attention given to the analyzed lines in section §2.1. Discussion of the DEM calculation procedure is given in §3 including concerns regarding scaling parameters in §3.1 and DEM validation in §3.2. The implications of this analysis on the Fe XVIII 94 Å line are discussed in §4 and we conclude and discuss future uses of these results in §5.

2. EVE MEGS-A Spectra

The Extreme ultraviolet Variability Experiment (EVE) includes a suite of instruments designed to observe the solar EUV irradiance with high cadence and accuracy. Within this suite, the Multiple EUV Grating Spectrographs (MEGS)-A grazing incidence spectrograph was designed to observe the solar irradiance at 50–370 Å with better than 1 Å resolution and greater than 25% accuracy every 10 seconds Woods et al. (2012). MEGS-A operated nearly continuously from 2010 April 30 until 2014 May 26 when it suffered a CCD failure (Pesnell 2014). There were four CCD bakeout procedures when no data was collected: 2010 June 16–18, 2010 September 23–27, 2012 March 12–13, and 2012 March 19–20.

We use the spectra collected between 19:00 and 20:59 UT and compute a daily median spectrum using only those data flagged as 'valid'. We choose to use the median in each spectral pixel to minimize the effects of short duration flares during the observation window. All of our analysis is performed with these daily median spectra.

2.1. Selected Emission Lines

The EVE MEGS-A instrument observed more than 150 unique emission features originating in the solar corona which are also contained in version 8 of the CHIANTI atomic line database (Dere et al. 1997; Del Zanna et al. 2015). In order to generate accurate and consistent DEMs from MEGS-A spectra we identify a short list of observed lines with properties suited to reliably calculate DEMs.

To simplify analysis we choose strong, relatively isolated emission features dominated by the emission from a single stage of Fe. We restrict analysis to Fe emission lines to eliminate uncertainty from elemental abundances (more detail in §3.1) due to lingering debate surrounding the coronal iron abundance in relation to the observed FIP effect (Feldman 1992; White et al. 2000; Asplund et al. 2009). Finally, lines are chosen with the intention of providing coverage of typical non-flaring coronal temperatures, with peak emission temperatures in the range $5.7 \leq \log(T) \leq 6.5$. The line list including peak temperatures, primary contributing lines, and relative line strengths is given in table 1 and the intensity per emission measure as functions of temperature are shown in Figure 1.

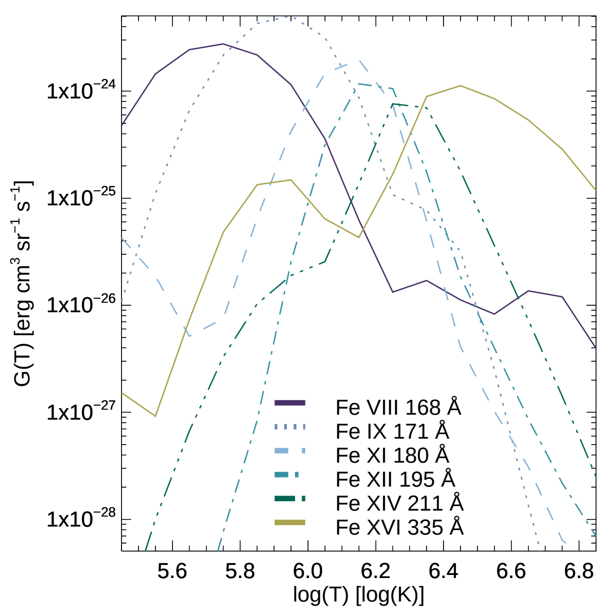

Fig. 1.—: The intensity per emission measure of the lines in table 1. This shows the temperature sensitivity of the individual emission lines and the combined sensitivity of the DEM. Notice that even though these lines (except for Fe XVI 335 Å) can be considered isothermal they have significant emission over a range of temperatures.

For the remainder of the text we refer to each line as an individual emission line but it must be noted that, because of the instrumental spectral

Table 1: EUV mission lines used to calculate DEMs

Ion	Wavelength [Å]	Peak [log(T)]	Relative Strength	Lower State	Upper State
Fe VIII	168.1720	5.75	$0.260, 1.315 \times 10^{-24}$	$3s^2\ 3p^6\ 3d\ ^2D_{5/2}$	$3s^2\ 3p^5\ 3d^2\ ^2D_{5/2}$
Fe VIII	167.6540	5.75	0.060	$3s^2\ 3p^6\ 3d\ ^2D_{3/2}$	$3s^2\ 3p^5\ 3d^2\ ^2D_{5/2}$
Fe VIII	168.0030	5.75	0.051	$3s^2\ 3p^6\ 3d\ ^2D_{5/2}$	$3s^2\ 3p^5\ 3d^2\ ^2D_{3/2}$
Fe VIII	168.5440	5.75	0.599	$3s^2\ 3p^6\ 3d\ ^2D_{5/2}$	$3s^2\ 3p^5\ 3d^2\ ^2P_{3/2}$
Fe VIII	168.9290	5.75	0.312	$3s^2\ 3p^6\ 3d\ ^2D_{3/2}$	$3s^2\ 3p^5\ 3d^2\ ^2P_{1/2}$
Fe IX	171.0730	5.95	$1.000, 5.048 \times 10^{-24}$	$3s^2\ 3p^6\ ^1S_0$	$3s^2\ 3p^5\ 3d\ ^1P_1$
Fe XI	180.4010	6.15	$0.349, 1.760 \times 10^{-24}$	$3s^2\ 3p^4\ ^3P_2$	$3s^2\ 3p^3\ 3d\ ^3D_3$
Fe X	180.4410	6.05	0.106	$3s^2\ 3p^5\ ^2P_{1/2}$	$3s^2\ 3p^4\ 3d\ ^2P_{1/2}$
Fe XII	195.1190	6.20	$0.257, 1.298 \times 10^{-24}$	$3s^2\ 3p^3\ ^4S_{3/2}$	$3s^2\ 3p^2\ 3d\ ^4P_{5/2}$
Fe XIV	211.3172	6.30	$0.182, 9.191 \times 10^{-25}$	$3s^2\ 3p\ ^2P_{1/2}$	$3s^2\ 3d\ ^2D_{3/2}$
Fe XVI	335.4090	6.45	$0.222, 1.123 \times 10^{-24}$	$3s\ ^2S_{1/2}$	$3p\ ^2P_{3/2}$
Mg VIII	335.2530	5.90	0.122	$2s^2\ 2p\ ^2P_{1/2}$	$2s\ 2p^2\ ^2S_{1/2}$

Emission lines identified in EVE MEGS-A spectra and used to compute DEMs. Each observed emission feature includes the primary line (the first line listed in each section) as well as all other lines within the full width half maximum of the primary line that have line strengths > 5% of the primary line. The "Relative Strength" column gives the intrinsic line strength corrected for the elemental abundance (but not weighted by a DEM) relative to the Fe IX line for the primary lines and relative to their respective primary lines for the secondary lines.

resolution (∼ 0.85 Å; Hock et al. 2012), each emission feature actually contains significant contributions from all lines within a resolution element of the primary line. In order to best extract the flux of each primary line we fit the emission features with three independent Gaussian functions, one at the primary wavelength and one each in the red and blue wings to account for the flux from neighbouring emission features. For each line except for Fe XII 195 Å, at least one of these wing line fits is close enough to the primary line that its peak is not visually identifiable. In these cases the width of these wing Gaussians is fixed to the width of the primary feature. A characteristic set of line fits are shown in Figure 2.

2.2. Excluded emission lines

There are of course many additional emission lines present in the EVE spectra which could, in principle, be used to calculate DEMs. We tested many of these in combination with the included lines but ultimately decided that at best they added nothing to the DEM and at worst they caused serious distortion in the calculated DEMs, reducing the self consistency of the other input lines. We instead decide to use the lines listed in table 2 to validate the calculated DEMs.

The chosen test lines span the temperature range of the lines used to compute the DEMs and test different properties of the solutions. Two of these test lines are Fe VIII 131 Å and Fe XI 188 Å which respectively validate the Fe VIII 168 Å and Fe XI 180 Å lines which are used in the DEM computations. The rest of the test lines are from stages of iron not included in the DEM calculations. These include Fe X 175 Å and Fe XV 284 Å which are both strong lines that could be expected to help constrain the DEM. However, the inclusion of either of these lines led to dramatic fluctuations in the DEM calculations and, as discussed in §3.2, they each show evidence of systematic errors associated with CHIANTI. The Fe XIII 202 Å and

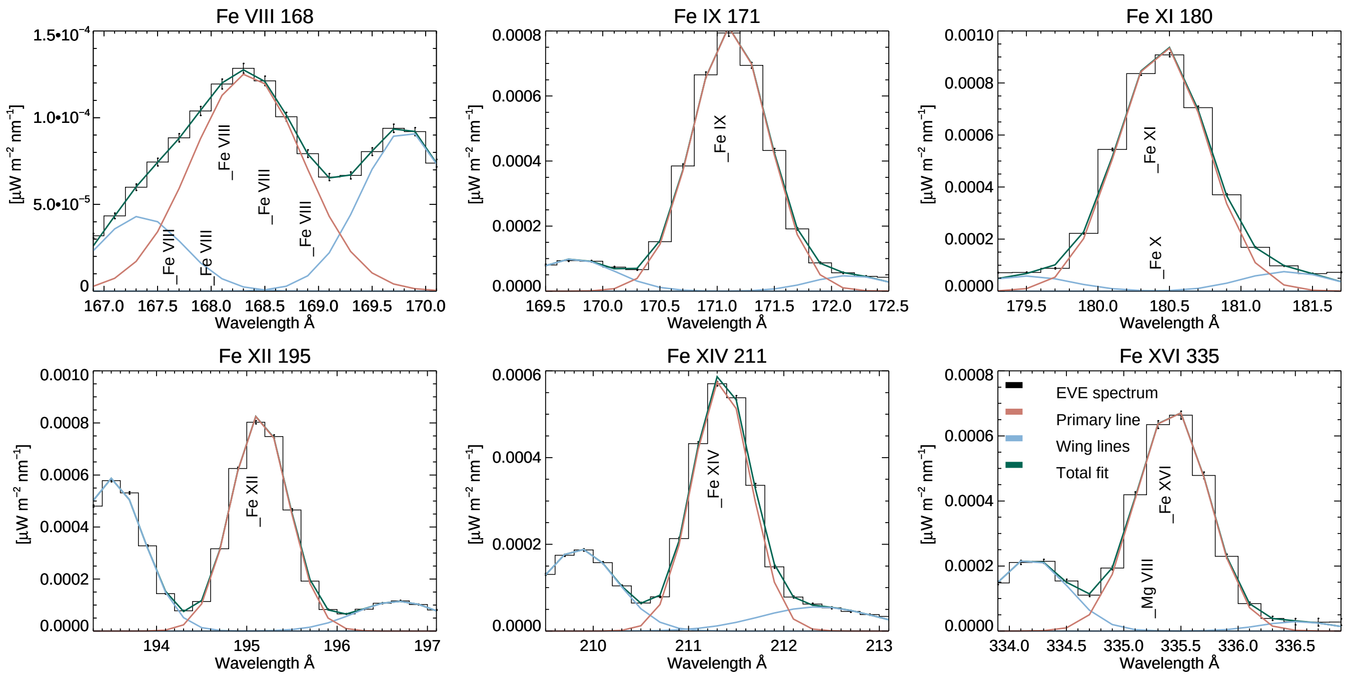

Fig. 2.—: The EVE spectrum and associated Gaussian fits for the lines in table 1 on 2011 December 9. The black line is the observed median EVE spectrum with error bars associated with statistical uncertainty and the variation in the spectrum over the two hour observation window. The red and blue lines are the Gaussian fits for the primary line and the wing features respectively. The green line is the total of all three fits which is matched to the observed spectrum. The lines listed in table 1 are also indicated at the proper wavelength and relative strength.

204 Å lines are known to be strongly density dependent and are included as a diagnostic of the density uncertainty discussed in §3.1. Finally, the Fe XVIII 94 Å line that is commonly used in active region and flare studies (e.g. Kennedy et al. 2013) is investigated in detail in §4.

3. The Differential Emission Measure

Using the line fluxes extracted from the MEGS-A spectra we generate daily full-disk-integrated coronal DEMs. These DEMs are made using version 8 of the CHIANTI database (Dere et al. 1997; Del Zanna et al. 2015), assuming coronal elemental abundances with Fe enhanced by a factor of 4 above the photospheric level (Feldman 1992), and a constant electron density of 1×10^9 cm^{-3}. We use the inversion DEM solution method from Hannah & Kontar (2012) which is incorporated in CHIANTI with a temperature range of $5.45 \leq \log(T) \leq 6.85$ and resolution of 0.1 and restricted the solutions to prevent unphysical negative emission measure. This method requires an estimation of the error in the observed line fluxes, and in order to ensure the algorithm is able to determine a physically meaning full solution we use three times the observed flux standard deviations. This helps compensate for the precise (leading to small standard deviations) but potentially low accuracy EVE observations as well as difficult to quantify uncertainties in CHIANTI.

The full four year DEM time series is plotted in Figure 3. These DEMs show the gradual increase from near solar minimum in 2010 to solar maximum in 2012–2014. During solar maximum there are times when a clear rotational modulation signal is present (particularly July 2012 – January 2013), showing a relatively longitudinally stable corona with strong active regions regularly rotating on and off the disk. However there are also times when the solar activity loses that regularity

Table 2: Test EUV emission lines excluded from DEM fits

Ion	Wavelength [Å]	Peak [log(T)]	Relative Strength	Lower State	Upper State
Fe VIII	131.2400	5.75	$0.047, 2.372 \times 10^{-25}$	$3s^2\ 3p^6\ 3d\ ^2D_{5/2}$	$3s^2\ 3p^6\ 4f\ ^2F_{7/2}$
Fe VIII	130.9410	5.75	0.668	$3s^2\ 3p^6\ 3d\ ^2D_{3/2}$	$3s^2\ 3p^6\ 4f\ ^2F_{5/2}$
Fe X	174.5310	6.05	$0.465, 2.348 \times 10^{-24}$	$3s^2\ 3p^5\ ^2P_{3/2}$	$3s^2\ 3p^4\ 3d\ ^2D_{5/2}$
Fe XI	188.2160	6.15	$0.171, 8.619 \times 10^{-25}$	$3s^2\ 3p^4\ ^3P_2$	$3s^2\ 3p^3\ 3d\ ^3P_2$
Fe XI	188.2990	6.15	0.602	$3s^2\ 3p^4\ ^3P_2$	$3s^2\ 3p^3\ 3d\ ^1P_1$
Fe IX	188.4930	5.95	0.277	$3s^2\ 3p^5\ 3d\ ^3F_4$	$3s^2\ 3p^4\ 3d^2\ ^3G_5$
Fe XIII	202.0440	6.25	$0.137, 6.936 \times 10^{-25}$	$3s^2\ 3p^2\ ^3P_0$	$3s^2\ 3p\ 3d\ ^3P_1$
Fe XI	201.7340	6.15	0.091	$3s^2\ 3p^4\ ^1D_2$	$3s^2\ 3p^3\ 3d\ ^3S_1$
Fe XI	202.4240	6.15	0.097	$3s^2\ 3p^4\ ^3P_2$	$3s^2\ 3p^3\ 3d\ ^3P_2$
Fe XIII	203.8260	6.25	$0.104, 5.251 \times 10^{-25}$	$3s^2\ 3p^2\ ^3P_2$	$3s^2\ 3p\ 3d\ ^3D_3$
Fe XII	203.7280	6.20	0.201	$3s^2\ 3p^3\ ^2D_{5/2}$	$3s^2\ 3p^2\ 3d\ ^2D_{5/2}$
Fe XIII	203.7950	6.25	0.402	$3s^2\ 3p^2\ ^3P_2$	$3s^2\ 3p\ 3d\ ^3D_2$
Fe XIII	204.2620	6.25	0.125	$3s^2\ 3p^2\ ^3P_1$	$3s^2\ 3p\ 3d\ ^1D_2$
Fe XV	284.1630	6.35	$0.499, 2.518 \times 10^{-24}$	$3s^2\ ^1S_0$	$3s\ 3p\ ^1P_1$
Fe XVIII	93.9322	6.85	$0.028, 1.436 \times 10^{-25}$	$2s^2\ 2p^5\ ^2P_{3/2}$	$2s\ 2p^6\ ^2S_{1/2}$
Fe VIII	93.4690	5.80	0.068	$3s^2\ 3p^6\ 3d\ ^2D_{3/2}$	$3s^2\ 3p^6\ 7f\ ^2F_{5/2}$
Fe XIV	93.6145	6.30	0.177	$3s^2\ 3d\ ^2D_{3/2}$	$3s^2\ 4p\ ^2P_{1/2}$
Fe VIII	93.6160	5.80	0.102	$3s^2\ 3p^6\ 3d\ ^2D_{5/2}$	$3s^2\ 3p^6\ 7f\ ^2F_{7/2}$
Fe XX	93.7811	7.00	0.064	$2s^2\ 2p^3\ ^2D_{5/2}$	$2s\ 2p^4\ ^2P_{3/2}$
Fe X	94.0120	6.05	0.292	$3s^2\ 3p^5\ ^2P_{3/2}$	$3s^2\ 3p^4\ 4s\ ^2D_{5/2}$

Same as Table 1 except that these emission lines were not used to calculate the DEMs.

and the rotational signal becomes obscured such as during June 2013 – November 2013. Figure 4 shows the emission measure binned by temperature for the whole data set and highlights the relative consistency of the low and medium temperature plasma relative to the high temperature plasma. The low temperature corona (< 1 MK) appears almost independent of the solar cycle, with very little change in emission measure due to either solar rotation or activity level. The mid temperatures (between 1 and 2.5 MK) which contain most of the emission measure show clear but relatively small variations with the solar rotation as well as a general increase over the near-solar-minimum level in 2010. The high temperature (> 2.5 MK) emission measure clearly shows the greatest variability, changing by over an order of magnitude. This is also demonstrated clearly in Figure 5 which shows the DEM during a period of low activity, moderately high activity, and their difference, which highlights the high temperature component of the DEM associated with coronal activity.

These DEMs are consistent with an intuitive understanding of a corona consisting of two primary components: the quiet Sun and active regions. The quiet Sun DEM component with a peak temperature of ~6.15 and little high temperature emission measure is present and relatively constant throughout the solar cycle. This suggests that, outside of active regions, there's no difference in the quiet Sun between solar minimum and maximum. The active region DEM component with a peak temperature of $sim6.25$ varies with the solar cycle as commonly anticipated. This component has more high temperature emission measure, and it is also highly variable, but whether or not this variability is dependent on

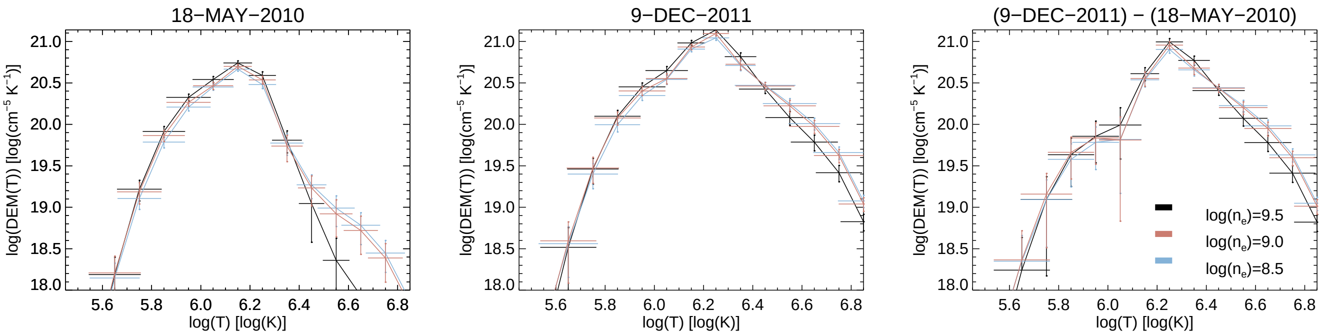

Fig. 5.—: DEMs for select days; *left*: the day with minimum observed emission measure, *middle* a characteristic high activity day, and *right:* the difference between the high and low activity DEMs. The different lines in each plot indicate the density assumed in the DEM (§3.1) and their spread gives an indication in the uncertainty of in the DEMs resulting from the choice of density. This effect is larger than the intrinsic errors within each DEM calculation, although still relatively minor, and appears to shift emission measure from the temperature extremes to the central $5.9 \leq \log(T) \leq 6.3$. The difference plot highlights the increased high temperature component of the DEM associated with coronal activity but shows that there is increased emission measure across all coronal temperatures.

3.1. CHIANTI scaling concerns

There are fundamental assumptions associated with the CHIANTI emission lines which impact the DEM results independently of the accuracy of the database itself. Specifically, the abundance and density assumptions warrant further discussion as each influences the intensity per emission measure functions shown in Figure 1 which are integral to the DEM calculation.

Because this method uses atomic emission to probe the electron density in the DEM, there is naturally an assumption regarding the relative number of electrons and the emitting elements. By using only emission lines from various stages of iron in our DEM calculations we have, to first order, simplified the influence of elemental abundances on the DEM down to a single value, the Fe abundance. This of course neglects the influence of secondary emission from other elements (such as the Mg VIII contribution to the Fe XVI line), but as these contributions are quite small their influence is likely negligible. This means that the DEM calculated from purely Fe emission lines scales inversely with the Fe abundance and the abundance has no influence on the shape of the DEM, assuming it is a constant. This analysis uses an iron abundance of $N_{Fe}/N_H = 1.26 \times 10^{-4}$, four times that of the photosphere (Feldman 1992), which Schonfeld et al. (2015) found suitable for full disk coronal analysis with emission dominated by active regions.

The effects of electron density are more complex since the density impacts individual emission lines differently. Electronic excitation (Gaetz & Salpeter 1983) and a fraction of the de-excitation in the corona is caused by electron–ion collisions (CITATION) whose rate is mediated by the electron density. Therefore, the rate at which individual excitation states within an ion are populated is a function of the electron density. Depending on the details of the excitation and de-excitation pathways for each individual transition, increased density can lead to decreased (through collisional quenching, CITATION) or increased (through collisional excitation, CITATION) emission. There is no guarantee that a change in density will cause the emission strengths of different lines to change in the same way, in fact many density diagnostics (Tripathi et al. 2008; Warren & Brooks 2009; Young et al. 2009) rely on oppositely signed changes in emission strength from lines produced by the same ionic stage. Because of this the density can have a dramatic effect on DEM derivation by changing the relative strengths of the theoretical line emission.

In order to account for the effects of density in our results we also performed the DEM calcu-

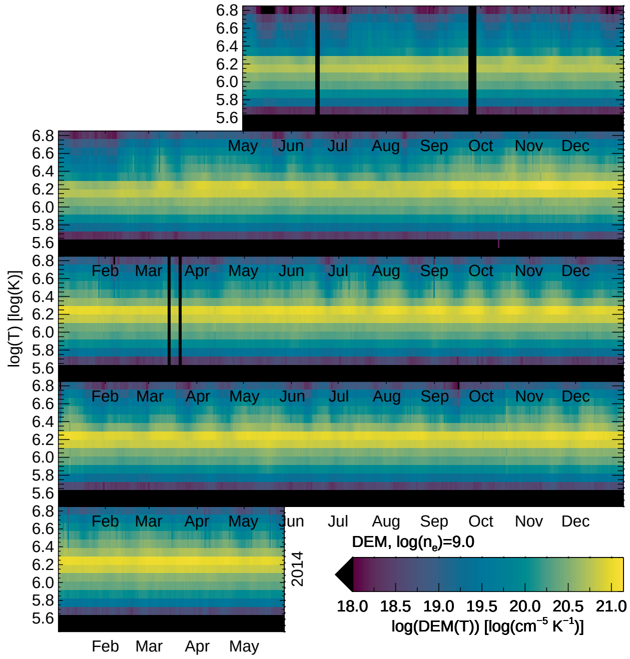

Fig. 3.—: The DEM time series calculated for the complete EVE data set. The vertical black bands in 2011 and 2012 are the result of data gaps explained in §2. The solar rotation (Carrington, R 1859) is seen clearly in July 2011 – February 2012.

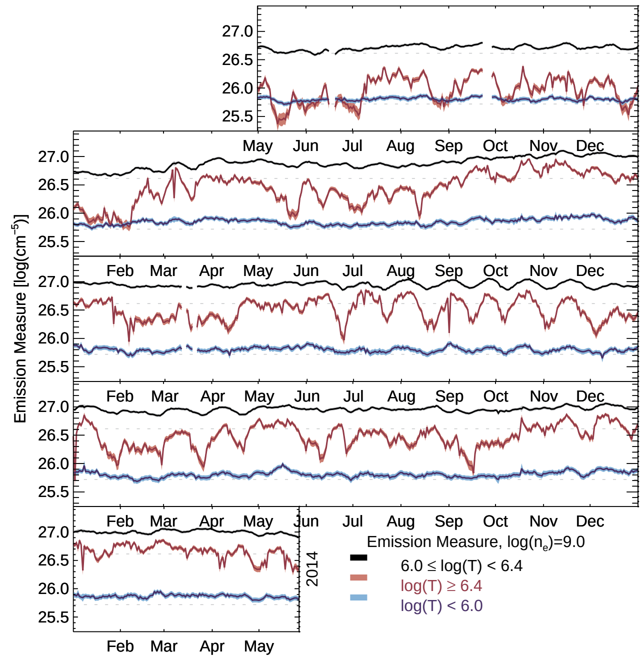

Fig. 4.—: The emission measure from figure 3 in the low (log(T)< 6.0), medium (6.0≤log(T)<6.4), and high (log(T)> 6.4) temperatures. The dashed horizontal lines mark the emission measure in the medium (top) and low (bottom) temperatures on 2010 May 18 which had the lowest total observed emission measure.

lations using $\log(n_e) = 8.5$ and 9.5 $\log(\mathrm{cm}^{-3})$. These values were chosen based on studies of the quiet Sun (Warren & Brooks 2009) and active regions (Tripathi et al. 2008; Young et al. 2009) as reasonable bounds for an average, full disk integrated electron density. It must be noted that testing in this way, with a single electron density for all lines, assumes a homogeneous corona where all ion species exist in identical plasma. This is almost certainly not the case as high temperature lines will preferentially emit in active regions where the density will be, in general, greater than the quiet sun where low temperature lines dominate. The alternative, computing DEMs with different electron densities for different emission lines, would likely not yield significantly improved results since each observed emission line will include contributions from plasma at a range of densities. However, even with all these complications, the results from these DEM calculations with different densities (Figure 5) demonstrate that while the density does have some effect on the DEMs, the overall shapes and total emission measures are very similar. The effect of increasing density seems to be to shift some of the emission measure from the temperature extremes to the middle of the temperature range. This is not unexpected since both Fe VIII 168 Å and Fe XVI 335 Å which sample low and high temperatures respectively are nearly density insensitive while the remaining, mid-temperature lines all have reduced emission with increased density. This means that in order to reproduce the same input flux there must be more emission measure in the mid-temperatures when a higher density is assumed.

3.2. DEM validation

To check the self-consistency of the DEMs we reproduced the input line fluxes by integrating over temperature the products of the intensity per emission measure profiles and the DEMs, i.e. the fluxes that would have been observed if the DEMs were correct. These reproduced fluxes are plotted against the input line fluxes in Figure 6. It is unsurprising that these fluxes are reproduced so well since it is this flux agreement which is optimized to arrive at the DEM. The line with the worst agreement is Fe VIII 168 Å which is consistently reproduced with less total intensity than observed, suggesting that the DEM might be underestimating the low temperature plasma. However, this line is the weakest and most blended line used in the DEM calculation. These effects combine to give it the largest relative errors and therefore the solution method will necessarily sacrifice accuracy in the Fe VIII 168 Å line to better fit the remaining lines. Even so, at $\log(n_e) = 9.0$ the output fluxes are consistent with the observations to within one standard deviation.

As a further test we generated similar comparisons (Figure 7) for the test emission lines listed in table 2 (excluding Fe XVIII 94 Å which is discussed in detail in §4) which were not used in the calculation of the DEMs. The reproduction of these test lines doesn't show the same level of agreement since they have no impact on the calculated DEMs, but they do reveal interesting trends that lend context to the results. The Fe VIII 131 Å line is very similar to the Fe VIII 168 Å line, showing that the reproduction of these two Fe VIII lines is consistent. The Fe X 175 Å line reproduction is confined to well within the statistical errors, but the trend is depressed more than two standard deviations from the observations. This could indicate a consistent underestimation of the emission measure at $\log(T) \sim 6.05$, but the similar temperature coverage of Fe IX and Fe XI (Figure 1) and the excellent reproduction of the Fe XI 188 Å line even though it wasn't used in the DEM calculation suggests instead problems in the CHIANTI database. Because this line is consistently underestimated, it's possible that CHIANTI is incomplete around 174.5 Å and that missing lines make up the flux difference between the observation and the reproduction. The Fe XIII 202 Å and 204 Å lines are known to have strong density dependence with the line intensities decreasing and increasing, respectively, with increasing density. The effects of the density sensitivity are obvious in Figure 7 where the reproduced flux in these lines changes as expected with density. Encouragingly, each of these lines suggests a density of $\log(n_e) = 8.5-9.0$, validating the choice of density range. Finally, opposite to the Fe X 175 Å line, the Fe XV 284 Å line is over predicted by about two standard deviations, although the scale of the intrinsic scatter is similar to the offset. This line dominates its region of the spectrum and therefore has very little contamination, meaning that this over prediction is a result of the calculated DEMs having excess emission measure at $\log(T) \sim 6.35$ or inaccuracies in the atomic physics used to calculate the line strength for the CHIANTI database.

4. Fe XVIII 94 Å

The Fe XVIII 94 Åline is a commonly used diagnostic of solar flares because it is the strongest EVE observed line generated by Fe XVIII, an ideal flare diagnostic because of its peak emission temperature of $\log(T) \sim 6.85$ which is above typical coronal temperatures but easily reached by even small flares (CITATION). This region of the spectrum is especially notable because of the Atmospheric Imaging Assembly (AIA Lemen et al. 2012) where the 94 Åbandpass is used as one of the primary diagnostics of high temperature plasma. Even so, it is well established that interpretation of these images is difficult due to the presence of lower temperature emission (Aschwanden & Boerner 2011; Reale et al. 2011; Boerner et al. 2012; Warren et al. 2012) and incompleteness in the CHIANTI database (Testa et al. 2012b; Aschwanden et al. 2013). These complications are often avoidable in flare studies where the pre-flare emission can be subtracted (e.g. Warren et al. 2013) to isolate only contributions from the high-temperature flare plasma which emits primarily in the well characterized Fe XVIII line.

Because our analysis focuses specifically on the non-flaring corona, this type of subtraction technique is inappropriate. We therefore investigate the spectrum surrounding the Fe XVIII 94 Å line to determine if the DEMs we calculate can reproduce the observed spectrum, or if EVE spectra are sufficient to identify missing CHIANTI lines. Figure 8 shows the observed and reproduced spectra, as well as the Gaussian fitted lines, for the two days previously analyzed, as well as four days with particularly large emission from the Fe XVIII

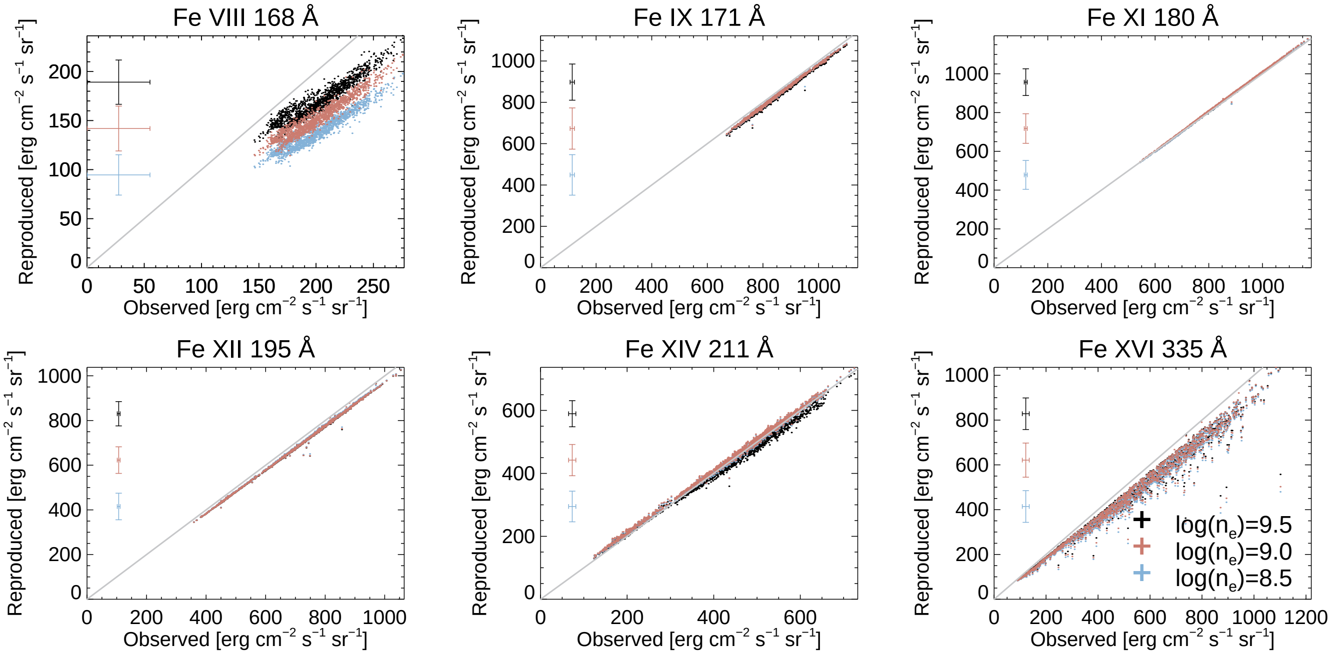

Fig. 6.—: The fluxes reproduced by the calculated DEMs vs. the observed flux for the lines in table 1 used to compute the DEMs. The diagonal gray lines indicate where the reproductions equal the observations. The clear density dependence of the Fe VIII 168 Å line reproduction is due to the combination of the relatively large errors which force most inaccuracies into this band, as well as its relatively density insensitivity while all the other lines (except Fe XVI 335 Å) decrease very similarly with increasing density.

line which indicates the presence of flares during the observation window. Unlike the other lines previously discussed, to fit the 94 Å region of the spectrum we simultaneously fit four Gaussians due to the clear emission features at 91.8, 92.9, 93.9, and 96 Å. The spectra recreated using the calculated DEMs and the lines included in CHIANTI are significantly reduced from what was observed by MEGS-A. This is unsurprising during flares since the lines used to compute the DEMs have little sensitivity to flare temperature plasmas and therefore the DEMs do not include much flare plasma. However, the fact that this effect spans all solar conditions and an order of magnitude in temperature suggests significant lines are missing from CHIANTI in this spectral window. This result is well documented (Teriaca et al. 2012; Testa et al. 2012b) and has led to empirical corrections in the AIA temperature response functions (**?**Boerner et al. 2014).

to determine if the Fe XVIII 94 Å line can be used reliably for non-flare studies.

5. Conclusion

Acknowledgements: S.W. would like to acknowledge valuable conversations with Ken Tapping. The National Radio Astronomy Observatory is a facility of the National Science Foundation operated under cooperative agreement by Associated Universities, Inc. We thank the Nobeyama Solar Radio Observatory for providing ready access to their data. Data supplied courtesy of the SDO/HMI and SDO/AIA consortia. SDO is the first mission to be launched for NASA's Living With a Star (LWS) Program. CHIANTI is a collaborative project involving George Mason University, the University of Michigan (USA) and the University of Cambridge (UK). This research has been made possible with funding from AFOSR FA9550-15-1-0014, NSF Career Award #1255024, New Mexico Space Grant (a NASA

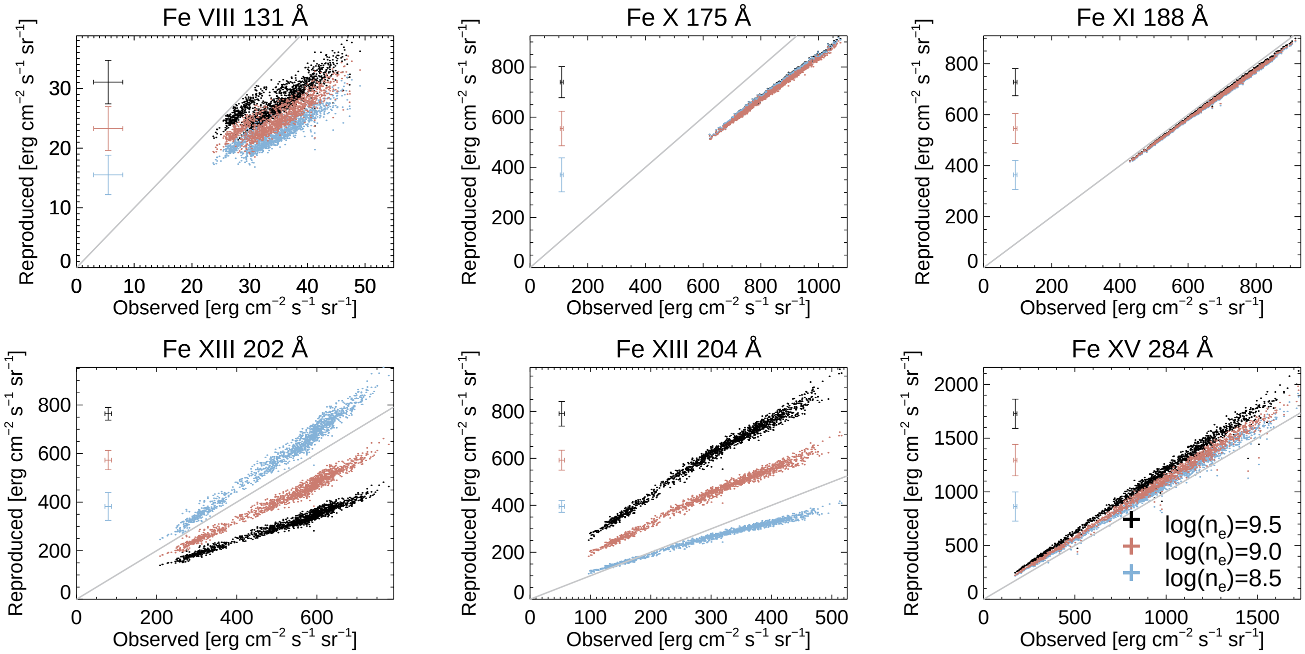

Fig. 7.—: The same as Figure 6 but for the lines in table 2 not used to compute the DEMs.

EPSCoR branch), and PAARE NSF:0849986.

REFERENCES

Aschwanden, M. J., & Boerner, P. 2011, The Astrophysical Journal, 732, 81

Aschwanden, M. J., Boerner, P., Caspi, A., et al. 2015, Solar Physics, 290, 2733

Aschwanden, M. J., Boerner, P., Schrijver, C. J., & Malanushenko, A. 2013, Solar Physics, 283, 5

Asplund, M., Grevesse, N., Sauval, a. J., & Scott, P. 2009, Annual Review of Astronomy and Astrophysics, 47, 481

Boerner, P., Edwards, C., Lemen, J., et al. 2012, Solar Physics, 275, 41

Boerner, P. F., Testa, P., Warren, H., Weber, M. A., & Schrijver, C. J. 2014, Solar Physics, 289, 2377

Carrington, R, C. 1859, Monthly Notices of the Royal Astronomical Society, 20, 13

Caspi, A., McTiernan, J. M., & Warren, H. P. 2014, The Astrophysical Journal Letters, 788, L31

Cheung, M. C. M., Boerner, P., Schrijver, C. J., et al. 2015, The Astrophysical Journal, 807, 143

Craig, I. J. D., & Brown, J. C. 1976, Astronomy & Astrophysics, 49, 239

Del Zanna, G. 2013, Astronomy & Astrophysics, 558, A73

Del Zanna, G., Dere, K. P., Young, P. R., Landi, E., & Mason, H. E. 2015, Astronomy & Astrophysics, 582, A56

Del Zanna, G., Dwyer, B. O., & Mason, H. E. 2011, Astronomy & Astrophysics, 535, 1

Dere, K. P., Landi, E., Mason, H. E., Monsignori Fossi, B. C., & Young, P. R. 1997, Astronomy and Astrophysics Supplement Series, 125, 149

Feldman, U. 1992, Physica Scripta Volume T, 46, 202

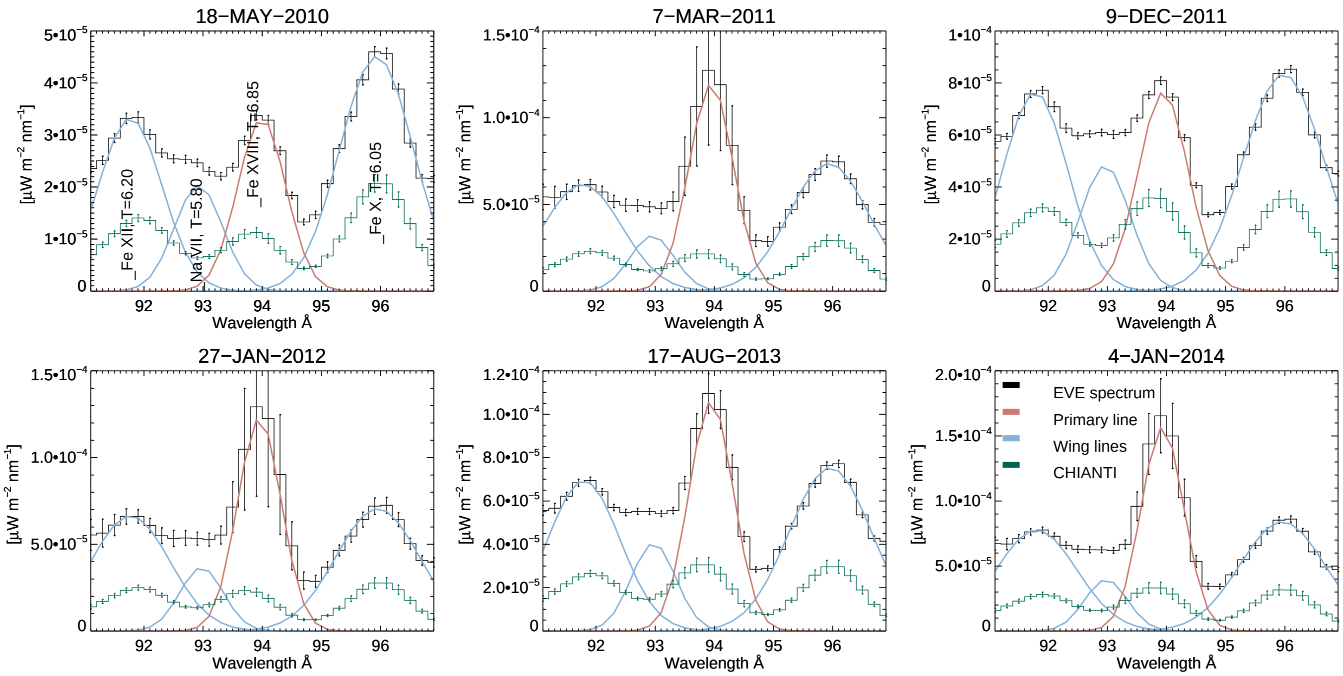

Fig. 8.—: The EVE MEGS-A spectrum, primary and wing line Gaussian fits, and reproduced spectrum of the region surrounding the Fe XVIII 94 Å line from the lines in CHIANTI. 2010 May 18 and 2011 December 9 are the same days shown in Figure 5 and the other four days shown all have flares (NEED TO CHECK ACTUAL FLARE LIST TO GENERATE THIS PLOT). The ion (and its characteristic temperature) responsible for the primary line contributing to each of the four Gaussians used to fit the spectrum is show in the 2010 May 18 plot.

Fletcher, L., Hannah, I. G., Hudson, H. S., & Innes, D. E. 2013, The Astrophysical Journal, 771, 104

Gaetz, T. J., & Salpeter, E. E. 1983, The Astrophysical Journal Supplement Series, 52, 155

Guennou, C., Auchère, F., Soubrié, E., et al. 2012a, The Astrophysical Journal Supplement Series, 203, 25

—. 2012b, The Astrophysical Journal Supplement Series, 203, 26

Hannah, I. G., & Kontar, E. P. 2012, Astronomy & Astrophysics, 539, A146

Hock, R. A. 2012, PhD thesis, University of Colorado at Boulder

Hock, R. a., Chamberlin, P. C., Woods, T. N., et al. 2012, Solar Physics, 275, 145

Hudson, H. S., Woods, T. N., Chamberlin, P. C., et al. 2011, Solar Physics, 273, 69

Kennedy, M. B., Milligan, R. O., Mathioudakis, M., & Keenan, F. P. 2013, The Astrophysical Journal, 779, 84

Lemen, J. R., Boerner, P. F., Edwards, C. G., et al. 2012, Sol. Phys., 275, 17

Milligan, R. O., Kennedy, M. B., Mathioudakis, M., & Keenan, F. P. 2012, The Astrophysical Journal Letters, 755, L16

Nuevo, F. A., Vásquez, A. M., Landi, E., & Frazin, R. 2015, The Astrophysical Journal, 811, 128

Pesnell, W. D. 2014

Pesnell, W. D., Thompson, B. J., & Chamberlin, P. C. 2011, Solar Physics, 275, 3

Petralia, a., Reale, F., Testa, P., & Del Zanna, G. 2014, Astronomy & Astrophysics, 564, A3

Plowman, J., Kankelborg, C., & Martens, P. 2013, The Astrophysical Journal, 771, 2

Reale, F., Guarrasi, M., Testa, P., et al. 2011, The Astrophysical Journal Letters, 736, L16

Schonfeld, S. J., White, S. M., Henney, C. J., Arge, C. N., & McAteer, R. T. J. 2015, The Astrophysical Journal, 808, 29

Teriaca, L., Warren, H. P., & Curdt, W. 2012, The Astrophysical Journal Letters, 754, L40

Testa, P., De Pontieu, B., Martínez-Sykora, J., Hansteen, V., & Carlsson, M. 2012a, The Astrophysical Journal, 758, 54

Testa, P., Drake, J. J., & Landi, E. 2012b, The Astrophysical Journal, 745, 111

Tripathi, D., Mason, H. E., Young, P. R., & Zanna, G. D. 2008, Astronomy & Astrophysics Special feature, 481, 53

Vázquez, A. M. 2016, Advances in Space Research, 57, 1286

Warren, H. P. 2014, The Astrophysical Journal Letters, 786, L2

Warren, H. P., & Brooks, D. H. 2009, The Astrophysical Journal, 700, 762

Warren, H. P., Brooks, D. H., & Winebarger, A. R. 2011, The Astrophysical Journal, 734, 90

Warren, H. P., Mariska, J. T., & Doschek, G. a. 2013, The Astrophysical Journal, 770, 116

Warren, H. P., Winebarger, A. R., & Brooks, D. H. 2012, The Astrophysical Journal, 759, 141

White, S. M., Thomas, R. J., Brosius, J., & Kundu, M. R. 2000, The Astrophysical Journal, 534, 203

Woods, T. N., Eparvier, F. G., Hock, R., et al. 2012, Solar Physics, 275, 115

Young, P. R., Watanabe, T., Hara, H., & Mariska, J. T. 2009, Astronomy & Astrophysics, 495, 587

Zhu, C., Liu, R., Alexander, D., & Mcateer, R. T. J. 2016, The Astrophysical Journal Letters, 821, L29

This 2-column preprint was prepared with the AAS LaTeX macros v5.2.

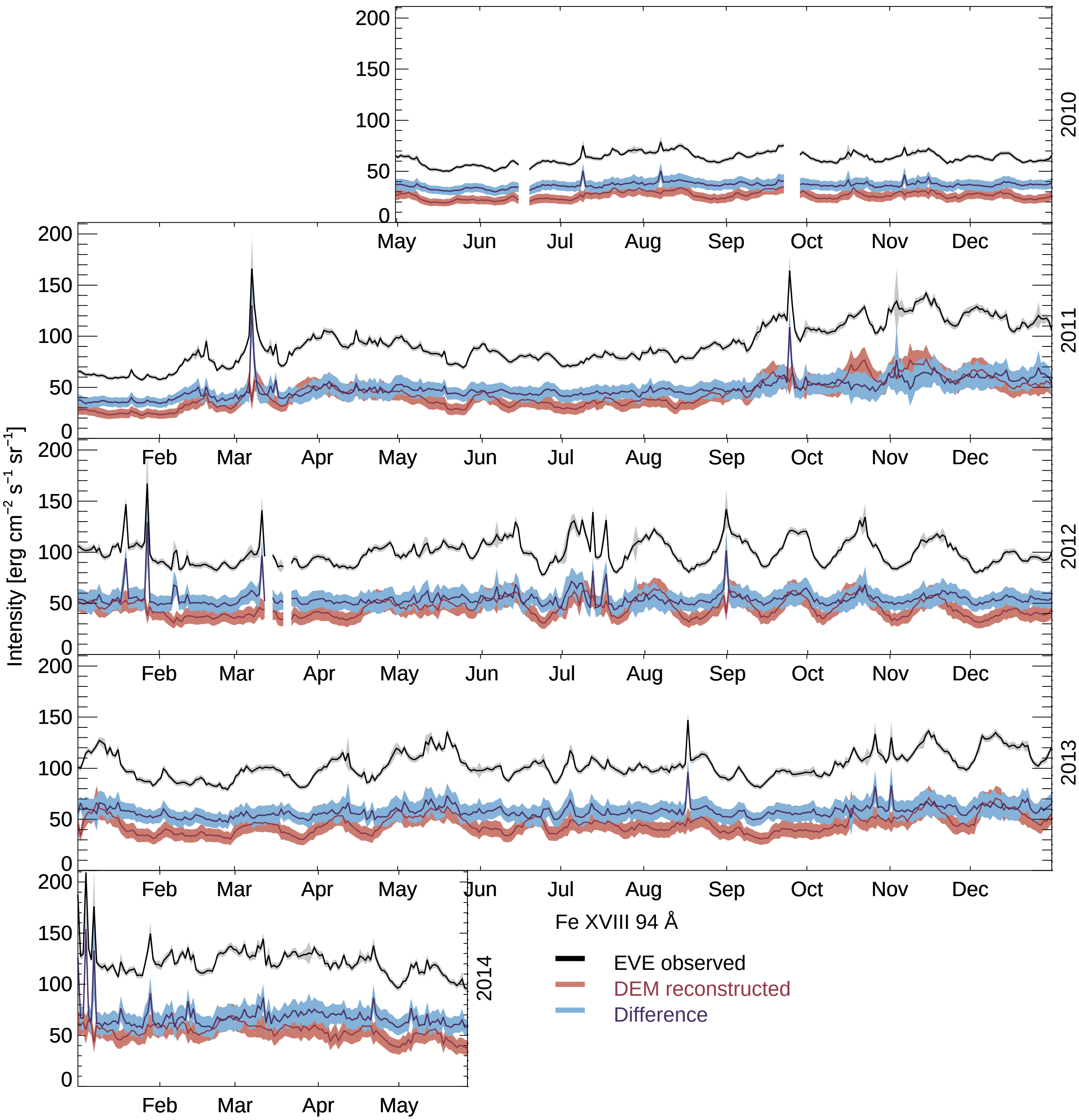

Fig. 9.—: The time series of the intensity in the Fe XVIII 94 Å line observed by MEGS-A, reproduced from the DEMs, and the difference between the observation and the reproduction. The sharp spikes in the observation and difference lines are flares with high temperature plasma which is not sampled by the lines used to compute the DEM for the mostly non-flaring Sun.